

# Meso-Scale Damage Simulation of 3D Braided Composites under Quasi-Static Axial Tension

Chao Zhang<sup>1</sup> · Chunjian Mao<sup>2</sup> · Yexin Zhou<sup>3</sup>

Received: 28 September 2016 / Accepted: 3 October 2016 / Published online: 4 January 2017  
© Springer Science+Business Media Dordrecht 2017

**Abstract** The microstructure of 3D braided composites is composed of three phases: braiding yarn, matrix and interface. In this paper, a representative unit-cell (RUC) model including these three phases is established. Coupling with the periodical boundary condition, the damage behavior of 3D braided composites under quasi-static axial tension is simulated by using finite element method based on this RUC model. An anisotropic damage model based on Murakami damage theory is proposed to predict the damage evolution of yarns and matrix; a damage-friction combination interface constitutive model is adopted to predict the interface debonding behavior. A user material subroutine (VUMAT) involving these damage models is developed and implemented in the finite element software ABAQUS/Explicit. The whole process of damage evolution of 3D braided composites under quasi-static axial tension with typical braiding angles is simulated, and the damage mechanisms are revealed in detail in the simulation process. The tensile strength properties of the braided composites are predicted from the calculated stress-strain curves. Numerical results agree with the available experiment data and thus validates the proposed damage analysis model. The effects of certain material parameters on the predicted stress-strain responses are also discussed by numerical parameter study.

---

✉ Chao Zhang  
zhangchao@ujs.edu.cn

✉ Chunjian Mao  
maochunjian@nuaa.edu.cn

Yexin Zhou  
caihui6871@163.com

<sup>1</sup> School of Mechanical Engineering, Jiangsu University, 301 Xuefu Road, Zhenjiang, Jiangsu 212013, China

<sup>2</sup> State Key Laboratory of Mechanics and Control of Mechanical Structures, Nanjing University of Aeronautics and Astronautics, 29 Yudao Street, Nanjing 210016, China

<sup>3</sup> Faculty of Civil Engineering and Mechanics, Jiangsu University, Zhenjiang, China

**Keywords** 3D braided composites · Representative unit-cell · Damage modeling · Strength prediction · Finite element analysis

## 1 Introduction

Laminated composites are being widely used in many industries because of their high performance-weight ratio. However, poor out-of-plane properties, low damage tolerance and high production costs have limited their application in primary loading-bearing structures. In the past two decades, 3D braided composites have received much attention due to their abundant advantages over the laminated composites. The distinct feature of 3D braided composites is the integrated near-net-shape structures, which can provide outstanding through-thickness mechanical properties. Due to these merits, 3D braided composites are believed to have broad potential application as the primary loading-bearing structures in the aeronautics and astronautics industries.

Before the application of 3D braided composites, a rational characterization of their mechanical properties is essential. The spatial configuration of the braiding yarns is complex, however, the microstructure of 3D braided composites shows a good periodicity. Therefore, a representative unit-cell (RUC) model is generally developed to investigate the mechanical properties of the materials and remarkable achievements have been obtained on the prediction of stiffness and strength properties.

Zeng et al. [1] established a multiphase finite element model to determine the stress field and tensile strength of 3D braided composites. Yu and Cui [2] predicted the stiffness and strength properties of 3D braided composites via a two-scale finite element method. Fang et al. [3] and Lu et al. [4] investigated the progressive damage behavior of 3D braided composites under uniaxial tension by introducing continuum damage theory. Dong and Feng [5] applied the asymptotic expansion homogenization method combined with the three unit-cells model to study the nonlinear tension response of 3D braided composites. Wang et al. [6] and Zhang et al. [7] developed the RUC-based finite element model to evaluate the strength characterizations of 3D braided composites under complex biaxial loadings. Similar works on damage analysis and strength prediction of braided composites have also been reported in references [8–11].

In the above research works, the interface was not considered in the RUC models. Thus, the interface debonding, which is a typical failure mode of 3D braided composites was ignored. Recently, with the rapid development of finite element simulation technology and the in-depth study of the micromechanical properties, the interface behavior of 3D braided composites has been subjected to special concern.

Fang et al. [12] proposed a RUC involving the interface damage model to predict the progressive damage evolution of 3D braided composites with large braiding angle. Lu et al. [13] discussed the effect of interfacial properties on the mechanical behavior of 3D braided composites. Xu et al. [14] developed a multi-layers micromechanical model to predict the elastic modulus of 3D multi-phase braided composites. In their model, the interfacial mechanical properties could be defined. By using X-ray tomography, Sharma et al. [15] constructed a microstructure model to predict the elastic properties of 3D carbon/carbon composites, in which frictional cohesive surfaces were used to model the yarn/matrix interfaces.

3D braided composites are composed of three phases: braiding yarn, resin matrix and interface. Up to now, few attempts have been made to establish a robust numerical damage

analysis model incorporate these three phases simultaneously with appropriate constitutive models. Meanwhile, the difficulties of convergence during the numerical calculation caused by severe damage of interface elements have not been studied well. In this paper, a RUC-based finite element model, which truly reflects the microstructure of 3D braided composites, is established. Coupling with the periodical boundary condition, the RUC is presented to simulate the damage propagation of 3D braided composites under quasi-static tension loadings. In this RUC model, a continuum damage model is proposed to predict damage evolution of yarns and matrix; a damage-friction combination interface constitutive model is applied to evaluate the debonding behavior of interface. All these constitutive models are coded by a user material subroutine VUMAT and implemented in the finite element software ABAQUS/Explicit. The whole process of damage initiation, propagation and final failure is carried out and the damage mechanisms in this process are revealed in detail. The effects of certain material parameters on the mechanical properties of 3D braided composites are also investigated.

The organization of the paper is as follows. Section 2 describes briefly the establishment of the RUC model of 3D braided composites. The damage evolution models of the three phases in 3D braided composites are given in section 3. The complete finite element model is described in section 4. Section 5 discusses the numerical results and reveals the damage mechanisms in detail. Finally, based on the results reported herein, some conclusions are drawn.

## 2 Unit-Cell Structural Model

3D braided composites are manufactured by braided preforms impregnated and consolidated with resin materials. 3D braiding preform is fabricated by four-step  $1 \times 1$  braiding technology. Each machine cycle consists of four movement steps of yarn carriers on the machine bed. After a machine cycle, a finite length of preform is obtained and called as a braiding pitch, denoted by  $h$ . Owing to the complexity of the architecture, a representative unit-cell (RUC) model is always established to study the mechanical properties of the composites. Through experimental observation, it is found by Chen et al. [16] that the braiding yarns axes remain straight and keep surface contact with each other due to mutual squeeze. A unit-cell structural model proposed by Xu et al. [17], which considered the contact and squeeze situation of yarns in 3D braided composites is employed here.

Figure 1 shows the unit-cell structural model of 3D braided composites. The cross-section shape of the braiding yarns is considered as octagon containing an inscribed ellipse. The relationship between the major and minor radii of the ellipse,  $a$  and  $b$ , is expressed as

$$a = \sqrt{3}b\cos\gamma \quad (1)$$

where  $\gamma$  is the interior braiding angle of 3D braided composites. As shown in Fig. 1,  $W$ ,  $T$  and  $h$  represent the width, thickness and height of the unit-cell model respectively, and they can be computed by

$$W = T = 4\sqrt{2}b \quad (2)$$

$$h = 8b/\tan\gamma \quad (3)$$

Generally, the interior braiding angle  $\gamma$  is difficult to measure since the interior of the preform cannot be observed without cutting the specimen. However, the angle of inclination of

the yarns on the surface of composites can be measured readily. The relationship between the braiding angle  $\alpha$  on the surface of composites and the interior braiding angle  $\gamma$  can be expressed as [16]

$$\tan \alpha = \left(\sqrt{2}/2\right)\tan \gamma \tag{4}$$

### 3 Progressive Damage Model of 3D Braided Composites

The progressive damage process can be simulated by damage model, which consists of damage initiation criteria and damage evolution law. The damage mechanism of 3D braided composites contains three types: yarn breaking, matrix cracking and interface debonding.

#### 3.1 Progressive Damage Model of Yarns and Matrix

##### 3.1.1 Damage Initiation Criteria

3D Hashin failure criterion [18] is one of the most well-known criteria for predicting the failure initiation of braiding yarns. In this paper, it will be adopted in the simulation. In the following equations, the  $L$ - $T$ - $Z$  rectangular coordinate is employed as the local coordinate definition of braiding yarn, where  $L$ -,  $T$ - and  $Z$ - axes indicate the longitudinal and two transverse directions. The 3D Hashin’s failure criterion is given by

Yarn tensile failure in  $L$  direction ( $\sigma_L \geq 0$ )

$$\varphi_{L_t} = \left(\frac{\sigma_L}{F_L^t}\right)^2 + \beta \left(\frac{\sigma_{LT}}{S_{LT}}\right)^2 + \beta \left(\frac{\sigma_{LZ}}{S_{LZ}}\right)^2 \geq 1 \tag{5}$$

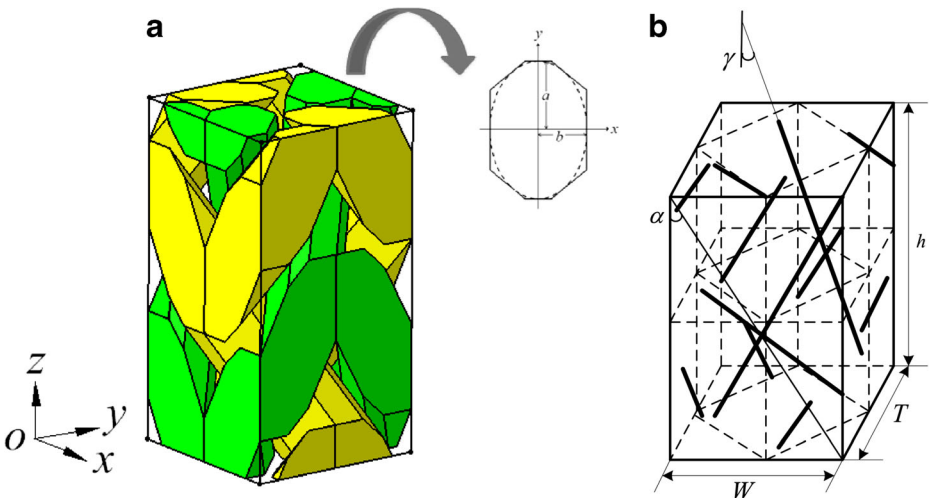


**Fig. 1** Unit-cell structural model **a** 3D model of unit-cell **b** Topological relationship of braiding yarns

Yarn compressive failure in  $L$  direction ( $\sigma_L < 0$ )

$$\varphi_{Lc} = \left(\frac{\sigma_L}{F_L^c}\right)^2 \geq 1 \tag{6}$$

Yarn tensile and shear failure in  $T$  and  $Z$  direction ( $\sigma_T + \sigma_Z \geq 0$ )

$$\varphi_{T(Z)t} = \left(\frac{\sigma_T + \sigma_Z}{F_T^t}\right)^2 + \left(\frac{1}{S_{TZ}^2}\right)(\sigma_{TZ}^2 - \sigma_T\sigma_Z) + \left(\frac{\sigma_{LT}}{S_{LT}}\right)^2 + \left(\frac{\sigma_{LZ}}{S_{LZ}}\right)^2 \geq 1 \tag{7}$$

Yarn compressive and shear failure in  $T$  and  $Z$  direction ( $\sigma_T + \sigma_Z < 0$ )

$$\begin{aligned} \varphi_{T(Z)c} = & \left(\frac{\sigma_T + \sigma_Z}{2S_{TZ}}\right)^2 + \left(\frac{\sigma_T + \sigma_Z}{F_T^c}\right) \left[ \left(\frac{F_T^c}{2S_{TZ}}\right)^2 - 1 \right] + \frac{1}{S_{TZ}^2}(\sigma_{TZ}^2 - \sigma_T\sigma_Z) + \left(\frac{\sigma_{LT}}{S_{LT}}\right)^2 \\ & + \left(\frac{\sigma_{LZ}}{S_{LZ}}\right)^2 \geq 1 \end{aligned} \tag{8}$$

In the above equations,  $F_L^t$  and  $F_L^c$  are the longitudinal tensile and compressive strengths of braiding yarn;  $F_T^t$  and  $F_T^c$  are the transverse tensile and compressive strengths;  $S_{LT}$ ,  $S_{LZ}$  and  $S_{TZ}$  are the  $LT$ ,  $LZ$  and  $TZ$  shear strengths, respectively.

In Eq. (5), the shear failure coefficient  $\beta$  ( $0 \leq \beta \leq 1$ ) is applied to determine the contribution of shear stresses on the yarn tensile failure in  $L$  direction. As pointed by Zhang et al. [9], the strength properties of the braided composites are sensitive to this coefficient under tension load. The inclusion of this shear coefficient can serve as a compensation of in-situ shear strength and free-edge-effect induced premature damage.

The maximum stress criterion is adopted as matrix initiation failure criterion, namely

$$\varphi_{Mt} = \left| \frac{\sigma_1^t}{F_m^t} \right| \geq 1 \tag{9}$$

$$\varphi_{Mc} = \left| \frac{\sigma_3^c}{F_m^c} \right| \geq 1 \tag{10}$$

where  $F_m^t$  and  $F_m^c$  are tensile and compressive strength of matrix;  $\sigma_1^t$  and  $\sigma_3^c$  are the maximum tensile and compressive stress of matrix.

### 3.1.2 Damage Evolution Model

The damage of yarns and matrix can be characterized by Murakami damage model [19]. The damage model uses three principal damage variables to express the damage station, which is expressed as

$$D = \sum_i D_i n_i \otimes n_i \quad (i = L, T, Z) \tag{11}$$

where  $D_i$  and  $n_i$  are the principal value and principle unit vector of damage tensor, respectively.

The principal damage variables range from 0 to 1.0 according to damage station.  $D_i = 0$  represents the initial undamaged materials and  $D_i = 1$  implies the completely damaged materials.

For yarns, the principal damage variables in  $L$ ,  $T$ , and  $Z$  direction, are given by

$$D_L = \max(d_{Lt}, d_{Lc}) \tag{12}$$

$$D_T = \max(d_{Tt}, d_{Tc}) \tag{13}$$

$$D_Z = \max(d_{Zt}, d_{Zc}) \tag{14}$$

For matrix, one has

$$D_L = D_T = D_Z = \max(d_{Mt}, d_{Mc}) \tag{15}$$

In the above equations,  $d_i(I = Lt, Lc, Tt, Tc, Zt, Zc)$  are the damage variables corresponding to six damage modes of braiding yarns;  $d_{Mt}$  and  $d_{Mc}$  are the damage variables corresponding to tension and compression damage of matrix, respectively.

The damage variable  $d_I$  to a particular mode can be calculated by damage evolution, defined as [20]

$$d_I = \frac{\delta_{1,eq}^f (\delta_{1,eq} - \delta_{1,eq}^0)}{\delta_{1,eq} (\delta_{1,eq}^f - \delta_{1,eq}^0)} \quad (I = Lt, Lc, Tt, Tc, Zt, Zc, Mt, Mc) \tag{16}$$

where  $\delta_{1,eq}^0$  is the initial equivalent displacement at which the failure criterion is satisfied.  $\delta_{1,eq}^f$  is the full equivalent displacement at which the material is completely failure. They can be computed by

$$\delta_{1,eq}^0 = \frac{\delta_{1,eq}}{\sqrt{\varphi_1}} \tag{17}$$

$$\delta_{1,eq}^f = \frac{2G_I}{\sigma_{1,eq} / \sqrt{\varphi_1}} \tag{18}$$

Here,  $\varphi_1$  is the value of damage initiation criterion,  $G_I$  is the fracture energy density.  $\delta_{1,eq}$  and  $\sigma_{1,eq}$  are the equivalent displacement and stress for a failure mode, respectively. Their expressions are similar to those given in references [4, 9] and are summarized in Table 1, where  $l_c$  is the characteristic length of the element.

For the damaged material, the effective stress is defined as

$$\sigma^* = \frac{1}{2} \left[ (I-D)^{-1} \sigma + \sigma (I-D)^{-1} \right] = M(D) \sigma \tag{19}$$

Here  $\sigma^*$  is symmetric and  $M(D)$  is a transformation matrix.

Next, the constitutive equation of the damaged material is given by

$$\varepsilon = H(D) \sigma \tag{20}$$

In the above equation,  $H(D)$  is derived by the notion of energy identification.

$$H(D) = (M(D))^T : C_0 : M(D) \tag{21}$$

where  $C_0$  is the undamaged elastic tensor.

This, in turn, leads to the damaged stiffness matrix, which is the function of the undamaged elastic constants and the principal values of damage tensor, as shown below [21]

$$C(D) = H^{-1}(D) = \left\{ \begin{array}{cccccc} b_L^2 C_{11} & 0 & 0 & 0 & 0 & 0 \\ b_L b_T C_{12} & b_T^2 C_{22} & 0 & 0 & 0 & 0 \\ b_L b_Z C_{13} & b_T b_Z C_{23} & b_Z^2 C_{33} & 0 & 0 & 0 \\ & sym & & b_{TZ} C_{44} & 0 & 0 \\ & & & & b_{ZL} C_{55} & 0 \\ & & & & & b_{LT} C_{66} \end{array} \right\} \quad (22)$$

In the above equation,

$$b_L = 1 - D_L, \quad b_T = 1 - D_T, \quad b_Z = 1 - D_Z$$

$$b_{TZ} = \left( \frac{2b_T b_Z}{b_T + b_Z} \right)^2, \quad b_{ZL} = \left( \frac{2b_Z b_L}{b_Z + b_L} \right)^2$$

$$b_{LT} = \left( \frac{2b_L b_T}{b_L + b_T} \right)^2$$

$C_{ij}$ , is the component of undamaged stiffness tensor.

After damage occurred, the yarn and matrix materials are still considered to be elastic and the damage response of the integration points are governed by the stiffness matrix reduction via updating damage variables given in Eq. (22).

### 3.2 Progressive Damage Model of Interface

The zero-thickness cohesive element is used to simulate the interface debonding in the yarn/matrix and yarn/yarn interfaces of 3D braided composites. The traction stress and separation displacement of the nodes on the interface are governed by traction-separation law. In general, the interface debonding growth is likely to occur under mixed-mode loading, and damage initiation and the corresponding reduction behavior may occur before any of the involved traction components reach their respective allowable values. In this paper, the mix-mode bilinear constitutive model of interface element proposed by Camanho et al. [22] is utilized. In order to describe the damage initiation and evolution under mixed-mode loading, the effective relative displacement,  $\delta_m$ , is introduced as

$$\delta_m = \sqrt{\langle \delta_1 \rangle^2 + \delta_2^2 + \delta_3^2} \quad (23)$$

Herein, the Macaulay bracket is used to indicate that the pure compressive load will not cause any damage.

A quadratic nominal stress criterion is used to control the damage initiation displacement, i.e.  $\delta_m^0$ , of the interface, which is given by

$$\left( \frac{\langle t_1 \rangle}{N} \right)^2 + \left( \frac{t_2}{S} \right)^2 + \left( \frac{t_3}{T} \right)^2 = 1 \quad (24)$$

where  $t_1$ ,  $t_2$  and  $t_3$  represent the normal and shear stresses, respectively.  $N$ ,  $S$  and  $T$  denote the interface tensile and shear strengths.

A interaction power law of the energy is applied to determine the final displacement, i.e.  $\delta_m^f$ , of the interface, which is given by

$$\left(\frac{G_I}{G_{IC}}\right)^2 + \left(\frac{G_{II}}{G_{IIC}}\right)^2 + \left(\frac{G_{III}}{G_{IIIC}}\right)^2 = 1 \tag{25}$$

where  $G_I$ ,  $G_{II}$  and  $G_{III}$  are current energy release rates of mode I, II and III while  $G_{IC}$ ,  $G_{IIC}$  and  $G_{IIIC}$  are critical fracture energies of mode I, II and III, respectively.

Defining the maximum relative displacement,  $\delta_m^{\max} = \max\{\delta_m^{\max}, \delta_m^f\}$ , the constitutive equation for interface element without consideration of friction is expressed as

$$t_s = D_{sr}\delta_r \quad (s = 1, 2, 3 ; r = 1, 2, 3) \tag{26a}$$

$$D_{sr} = \begin{cases} \bar{\delta}_{sr}K & (\delta_m^{\max} \leq \delta_m^0) \\ \bar{\delta}_{sr}(1-d)K & (\delta_m^0 < \delta_m^{\max} < \delta_m^f, \delta_1 > 0) \\ \bar{\delta}_{sr}[(1-d)K + Kd\bar{\delta}_{s1}] & (\delta_m^0 < \delta_m^{\max} < \delta_m^f, \delta_1 \leq 0) \\ 0 & (\delta_m^{\max} \geq \delta_m^f, \delta_1 > 0) \\ \bar{\delta}_{s1}\bar{\delta}_{1r}K & (\delta_m^{\max} \geq \delta_m^f, \delta_1 \leq 0) \end{cases} \tag{26b}$$

where  $K$  represents the initial stiffness of the interface and  $\bar{\delta}_{ij}$  is the Kronecker operator. The damage evolution function  $d$ , is expressed by

$$d = \frac{\delta_m^f(\delta_m^{\max} - \delta_m^0)}{\delta_m^{\max}(\delta_m^f - \delta_m^0)} \quad d \in [0, 1] \tag{27}$$

In this paper, the influence of the friction force on the interface response is considered. The traction on the interface element is the sum of traction  $\tau_s$  determined by Eq. (26) and friction  $\tau_f$  generated on the damaged interface, namely [23]

$$\tau = \tau_s + \tau_f \tag{28}$$

The detail expression of friction force is expressed as follows.

$$\tau_{fr} = \begin{cases} \tau_{f1} = 0 & (\delta_1 \geq 0) \\ 0 & (\delta_m^{\max} \leq \delta_m^0, \delta_1 < 0) \\ -\mu K d \delta_1 \delta_r / |\delta_r| & (\delta_m^0 < \delta_m^{\max} < \delta_m^f, \delta_1 < 0) \\ -\mu K \delta_1 \delta_r / |\delta_r| & (\delta_m^{\max} \geq \delta_m^f, \delta_1 < 0) \end{cases} \quad (r = 2, 3) \tag{29}$$

where  $\mu$  is the interface friction coefficient.

## 4 Finite Element Model

### 4.1 Periodic Boundary Conditions and Finite Element Meshing

3D braided composites are regarded as periodic structures consisting of periodic array of unit-cells. In order to obtain more reasonable micro-mechanical response, the unified periodical



**Table 1** Equivalent displacement and stress of different failure modes

Failure modes	Equivalence displacement	Equivalence stress
L tension ( $\sigma_{11} \geq 0$ )	$\delta_{L,eq} = l_c \sqrt{\langle \varepsilon_{11} \rangle^2 + \beta \varepsilon_{12}^2 + \beta \varepsilon_{13}^2}$	$l_c (\langle \sigma_{11} \rangle \langle \varepsilon_{11} \rangle + \beta \sigma_{12} \varepsilon_{12} + \beta \sigma_{13} \varepsilon_{13}) / \delta_{L,eq}$
L compression ( $\sigma_{11} < 0$ )	$\delta_{Lc,eq} = l_c \langle -\varepsilon_{11} \rangle$	$l_c \langle -\sigma_{11} \rangle \langle -\varepsilon_{11} \rangle / \delta_{Lc,eq}$
T tension ( $\sigma_{22} \geq 0$ )	$\delta_{T,eq} = l_c \sqrt{\langle \varepsilon_{22} \rangle^2 + \varepsilon_{12}^2 + \varepsilon_{23}^2}$	$l_c (\langle \sigma_{22} \rangle \langle \varepsilon_{22} \rangle + \sigma_{12} \varepsilon_{12} + \sigma_{23} \varepsilon_{23}) / \delta_{T,eq}$
L compression ( $\sigma_{22} < 0$ )	$\delta_{Tc,eq} = l_c \sqrt{\langle -\varepsilon_{22} \rangle^2 + \varepsilon_{12}^2 + \varepsilon_{23}^2}$	$l_c (\langle -\sigma_{22} \rangle \langle -\varepsilon_{22} \rangle + \sigma_{12} \varepsilon_{12} + \sigma_{23} \varepsilon_{23}) / \delta_{Tc,eq}$
Z tension ( $\sigma_{33} \geq 0$ )	$\delta_{Z,eq} = l_c \sqrt{\langle \varepsilon_{33} \rangle^2 + \varepsilon_{13}^2 + \varepsilon_{23}^2}$	$l_c (\langle \sigma_{33} \rangle \langle \varepsilon_{33} \rangle + \sigma_{13} \varepsilon_{13} + \sigma_{23} \varepsilon_{23}) / \delta_{Z,eq}$
Z compression ( $\sigma_{33} < 0$ )	$\delta_{Zc,eq} = l_c \sqrt{\langle -\varepsilon_{33} \rangle^2 + \varepsilon_{13}^2 + \varepsilon_{23}^2}$	$l_c (\langle -\sigma_{33} \rangle \langle -\varepsilon_{33} \rangle + \sigma_{13} \varepsilon_{13} + \sigma_{23} \varepsilon_{23}) / \delta_{Zc,eq}$
Matrix tension ( $\sigma_1 \geq 0$ )	$\delta_{Mt,eq} = l_c  \varepsilon_1 $	$l_c  \sigma_1   \varepsilon_1  / \delta_{Mt,eq}$
Matrix compression ( $\sigma_3 < 0$ )	$\delta_{Mc,eq} = l_c  \varepsilon_3 $	$l_c  \sigma_3   \varepsilon_3  / \delta_{Mc,eq}$

displacement boundary conditions proposed by Xia et al. [24] will be employed to combine with the damage simulation model in this paper. The general formulas of the boundary conditions are given as:

$$u_i = \bar{\varepsilon}_{ik} x_k + u_i^* \tag{30}$$

$$u_i^{j+} = \bar{\varepsilon}_{ik} x_k^{j+} + u_i^* \tag{31}$$

$$u_i^{j-} = \bar{\varepsilon}_{ik} x_k^{j-} + u_i^* \tag{32}$$

$$u_i^{j+} - u_i^{j-} = \bar{\varepsilon}_{ik} (x_k^{j+} - x_k^{j-}) = \bar{\varepsilon}_{ik} \Delta x_k^j \tag{33}$$

In Eq. (30),  $\bar{\varepsilon}_{ik}$  is the average strain of the unit-cell;  $u_i^*$  is the periodic part of the displacement components on the boundary surfaces and it is generally unknown. For a unit-cell, the displacements on a pair of parallel opposite boundary surfaces (denoted as “j+” and “j-”) can be expressed as in Eq. (31) and Eq. (32). Eq. (33) represents the difference between Eq. (31) and Eq. (32). Since  $\Delta x_k^j$  are constants for each pair of boundary surfaces, once  $\bar{\varepsilon}_{ik}$  is specified, the right side of Eq. (33) becomes constant. Eq. (33) does not contain the periodic part of the displacement components and can be carried out easily in the finite element analysis by setting the nodal displacement using linear constraint equations.

In order to satisfy the periodicity, the node distributions in the opposite paired faces of the unit-cell should be identical. The map meshing method is used in the surface mesh and the periodic boundary conditions are imposed on the paired nodes by a FORTRAN pre-compiler code.

Due to the complexity of the microstructure of 3D braided composites, mesh generation is an extremely difficult task when the interface is considered. Herein, 3D solid tetrahedral element (C3D4) available in ABAQUS is adopted for the discretization of yarns and matrix because of its geometry adaptability. Actually, it is difficult to generate zero-thickness cohesive elements in complicated microstructure directly by general finite element software or mesh generation tools. Therefore, another FORTRAN pre-compiler code involving the cohesive element generation is written and implemented to modify the INP model file in ABAQUS. Through this way, the zero-thickness cohesive elements (COH3D6) in the yarn/matrix and yarn/yarn interfacial zones are introduced in the unit-cell model of 3D braided composites. The finite element mesh of unit-cell of 3D braided composites is shown in Fig. 2.

In the model, the element size keeps small at the edges intersecting braiding yarns and resin matrix, and relative small element size is also required to obtain more accurate stress distribution, especially near the intersection boundaries of the RUC. In this study, the quality of the mesh is ensured by performing a mesh sensitivity analysis and checking the element distortion.

## 4.2 Material Properties of Constituents

The material response of the constituents directly influences the macro-mechanical behavior of the braided composites. In this work, the resin matrix is assumed to be isotropic; the braiding yarns containing thousands of fibers and matrix are modeled as transversely isotropic material in the local material coordinate system. The local material coordinate systems 1–2–3 are defined for the braiding yarn. Local 1-axis follows the yarn centerline and local 3-axis is in the upright plane perpendicular to the  $x$ - $y$  plane of the global coordinate, as shown in Figs. 1a and 3. In Fig. 3, 2-axis is removed for clarity. The stiffness and strength properties of the braiding yarns can be calculated using the rule of mixture given by Chamis [25].

## 4.3 Homogenization of Unit-Cell

To obtain the macroscopic stress-strain curve of the composites, the homogenization approach is employed. The stress-strain relationship of a unit-cell can be computed by

$$\bar{\sigma}_i = E_{ij} \bar{\varepsilon}_j \quad (34)$$

Once the global strain  $\bar{\varepsilon}_{ij}$  is applied in the finite element analysis by Eq. (33), the stress distribution of the unit-cell can be obtained, and the global stress  $\bar{\sigma}_{ij}$  can be determined by

$$\bar{\sigma}_{ij} = \frac{1}{V} \int_V \sigma_{ij} dV \quad (35)$$

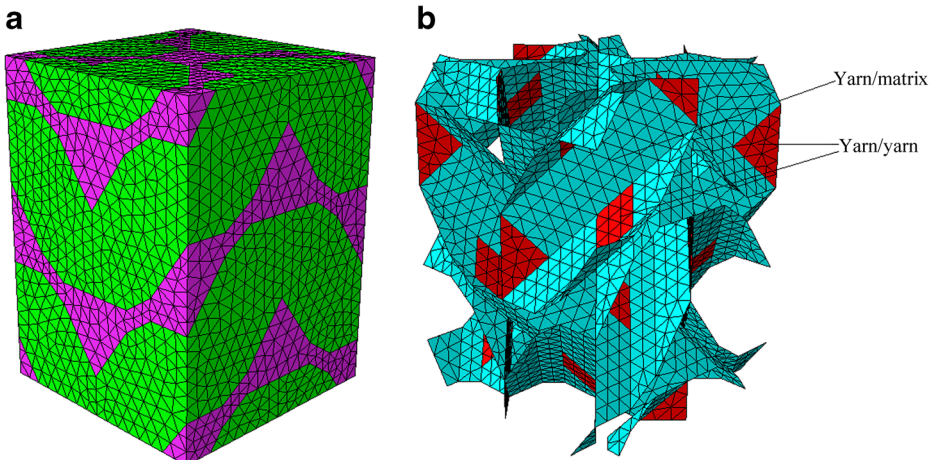


**Fig. 2** Finite element mesh of unit-cell **a** Unit-cell mesh **b** Interface mesh

The global stresses can be related to the ratios of resultant traction forces on the boundary surfaces to corresponding areas of the boundary surfaces, namely

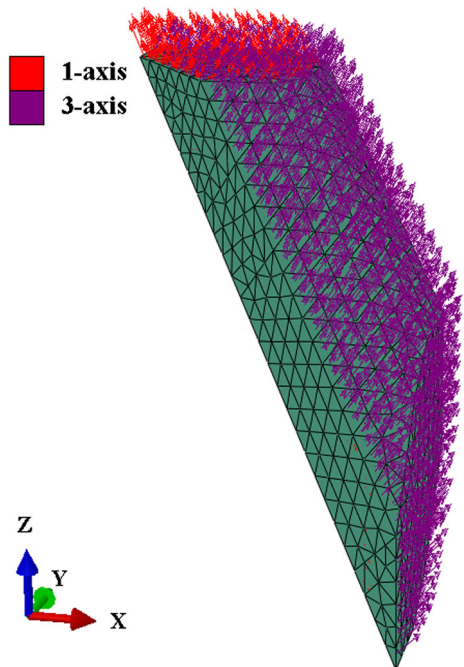
$$\bar{\sigma}_{ij} = \frac{(P_i)_j}{S_j} \quad (\text{no summation over } j) \quad (36)$$

where  $(P_i)_j$  is the  $i$ th resultant forces on the  $j$ th boundary surface and  $S_j$  is the area of the  $j$ th boundary surface.

#### 4.4 Damage Analysis Process

For the explicit progressive damage analysis of the unit-cell model subjected to tensile loads, the simulation process consists of two parts: the stress calculation and damage analysis. In order to conduct this analysis process, the constitutive model of each constituent, the failure criteria and the damage evolution model are implemented by using the user-defined material subroutine (VUMAT) available in ABAQUS with FORTRAN code. During each time increment, ABAQUS transmits the information of strain increments to VUMAT. With the constitutive models, the stress level and damage state in each constituent of the unit-cell can be obtained. Once the failure criterion is satisfied, the material properties reduction is carried out by updating the damage variables. The stresses at the integration points of elements are updated by using the reduced stiffness matrix. Finally, the updated state variables are returned to ABAQUS for next step analysis. Figure 4 presents the flow chart of the damage analysis process.

**Fig. 3** Material orientation definition of a braiding yarn



## 5 Results and Discussion

In order to verify the proposed damage simulation method and reveal the damage mechanisms of 3D braided composites under quasi-static axial tension, the tensile experiment results of two specimens with typical braiding angles (specimen 1 is  $19.2^\circ$  and specimen 2 is  $36.6^\circ$ ) from reference [26] are selected for comparisons. The braiding preforms of specimens herein are fabricated by four-step  $1 \times 1$  procedure. The finite element model of specimen 1 consists of 31, 943 nodes, 129, 686 C3D4 elements and 14, 388 COH3D6 elements; the finite element model of specimen 2 consists of 11, 143 nodes, 40, 811 C3D4 elements and 5, 926 COH3D6 elements. Table 2 gives the geometric parameters of the specimens and the structure parameters of the unit-cell models. The material properties of all the constituents are listed in Table 3.

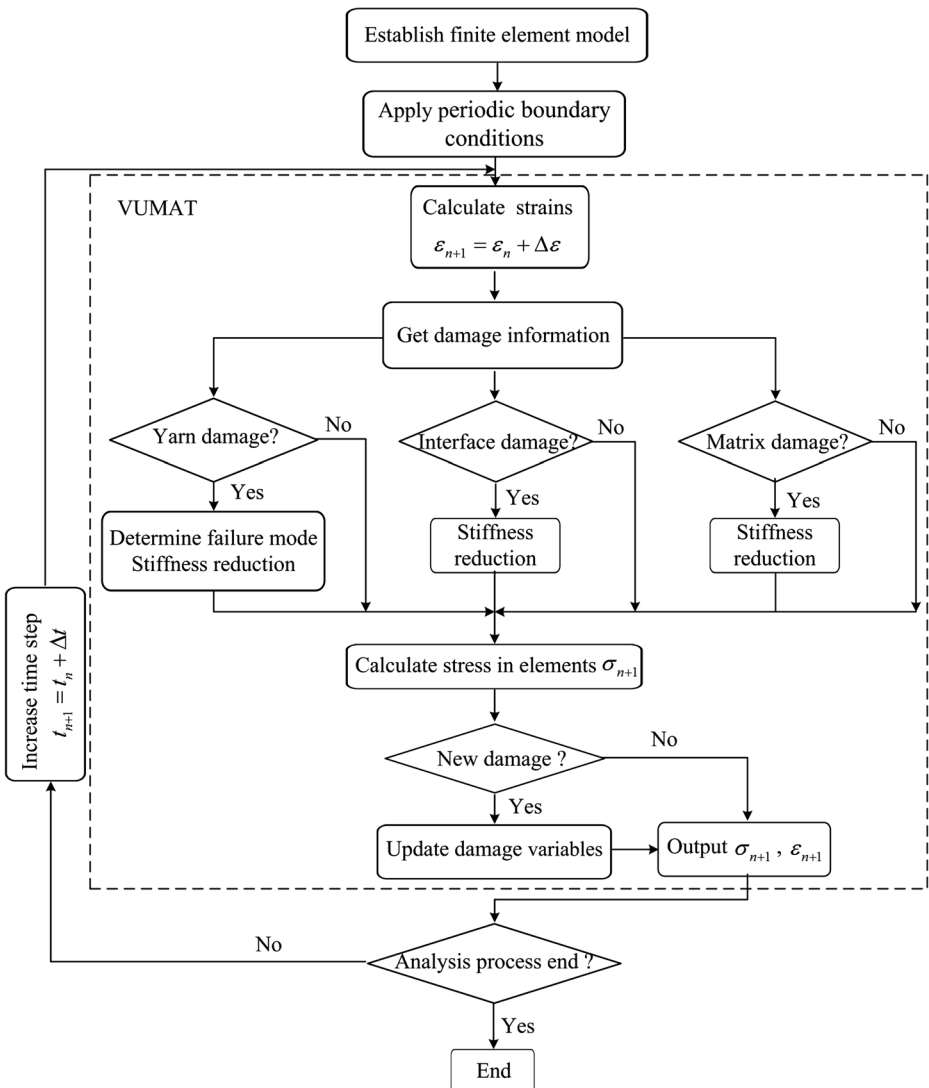
### 5.1 Tensile Stress-Strain Curves

Figure 5 illustrates the comparison of experimental and predicted stress-strain curves of two specimens with typical braiding angles under axial tension loads. Note that due to the brittle breaking characteristics of carbon-fiber reinforced braided composites, the experimental stress-strain curves stop after reaching the peak stresses. As shown in Fig. 5a, the computed stress-strain curves of specimen 1 with a small braiding angle keep approximately linear response before reaching the peak stresses and this linear feature is consistent with the experimental data. After reaching the peak stresses, the computed curves decrease rapidly thus the material loss the load-bearing capacity suddenly. As shown in Fig. 5b, the computed stress-strain curves of specimen 2 with a large braiding angle present some extent nonlinear feature before reaching the peak stresses. The nonlinear feature is due to the effects of local damage propagation. After reaching the peak stresses, the computed curves decrease gradually. The accumulation of various damage modes leads to the final failure of the material. Actually, once the stress-strain curves reach the peak stresses, the test specimens would break immediately. However, for finite element calculation, the extended unloading process observed in the computed stress-strain curves is a numerical technique, which can promote the numerical stability and display the continuing damage evolution process of the composites.

Table 4 presents the comparison of predicted tensile strength and failure strain with experiment data. For specimen 1, the tensile strength and fracture strain predicted by the unit-cell model with interface are larger than that without interface. For specimen 2, the prediction results obtained from these two models are very close. However, it can be found that the numerically predicted tensile strengths are always larger than the experiment data. This can be attributed to the initial geometrical and manufacturing defects, such as voids, micro-crack, fiber misalignment, and etc., which are not considered in the present meso-scale finite element models. Overall, the predicted results fit with the experimental data, which indicates that the proposed damage analysis model is reasonable. It deserves mentioning that even the meso-scale models with and without interface both provide reasonable stress-strain response, the interface debonding can only be simulated thoroughly by the RUC model considering interface.

### 5.2 Damage Evolution Mechanism Analysis

During the simulation, the damage mechanisms in 3D braided composites, such as yarn breaking, matrix cracking and interface debonding, can be captured by the proposed modeling



**Fig. 4** Flow chart of numerical analysis process

strategy. For specimen 1 with a small braiding angle, the main failure mode of braiding yarn is *L* tensile failure; while for specimen 2 with a large braiding angle, the main failure mode is yarn *T* compressive shear and *Z* tensile shear failure. Herein, only the damage evolution of interface debonding, yarn *L* tensile failure and matrix cracking are noted for specimen 1, as

**Table 2** Geometric parameters of the specimens and the structure parameters of the unit-cell models

Specimen	Yarn	Dimensions (mm)	$\alpha(^{\circ})$	$\gamma(^{\circ})$	$W(\text{mm})$	$h(\text{mm})$	$V_f(\%)$
Specimen 1	12 K	20.6×6.32×250	19.2	26.2	1.904	5.473	60.69
Specimen 2	6 K	20.6×8.58×250	36.6	46.4	1.662	2.239	52.04

**Table 3** Material properties of the constituents

	$E_{11}$ (GPa)	$E_{22}$ (GPa)	$G_{12}$ (GPa)	$G_{23}$ (GPa)	$\mu_{12}$	$K$ (N/mm <sup>3</sup> )	$\chi_T$ (MPa)	$\chi_C$ (MPa)	$S$ (MPa)	$G_L$ (N/mm)	$G_T$ (N/mm)	$G_m$ (N/mm)	$G_{IC}$ (N/mm)	$G_{IIC}$ (N/mm)
T300	230	40	24	14.3	0.26		3528	2470		8.0	1.5			
Matrix	3.5				0.35	$10^6$	80	241	60			1.0	0.306	0.632
Interface							80	60						

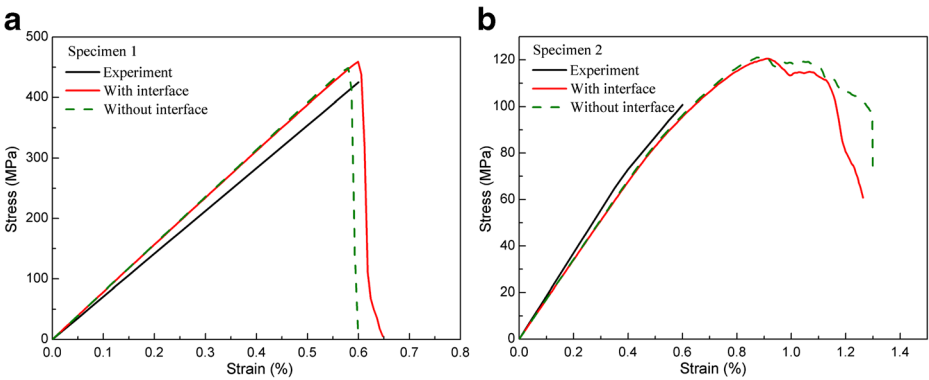


**Fig. 5** Comparison of experimental and predicted results under axial tension loads **a** Specimen 1 **b** Specimen 2

shown in Fig. 6, while only the damage evolution of interface debonding, yarn *T* compressive shear failure and matrix cracking are noted for specimen 2, as shown in Fig. 7. It is observed that the stress concentration is serious in the interlaced zones of braiding yarns under axial tension, and thus the micro-cracks and damage always generate in these regions. Therefore, in order to clearly demonstrate the damage distribution and development in the braiding yarns, the damage evolution process in one-directional yarns are given here, as shown in Fig. 6b and 7b.

For specimen 1, the main failure modes are yarn *L* tensile failure, yarn *Z* tensile shear failure, matrix cracking and interface debonding. At  $\bar{\epsilon}_z = 0.20\%$ , the interface debonding occurs first in the yarn/yarn contact zones near the top and bottom surfaces of the unit-cell. Then the interface debonding initiates in the yarn/yarn contact zones around the external boundaries of the unit-cell, as shown in Fig. 6a. With the increase of the axial tensile load, the interface damage gradually extends in the yarn/yarn contact zones inside the unit-cell and the extension speed gradually increases. At  $\bar{\epsilon}_z = 0.57\%$ , yarn *L* tensile failure starts in the braiding yarn and stimulates the yarn *Z* tensile shear failure and initial damage of the matrix, as shown in Fig. 6b, c. At  $\bar{\epsilon}_z = 0.60\%$ , the stress-strain curve reaches the peak value. At this point, except for the interface damage, the number of damage elements in the braiding yarns and matrix is relatively small. Thereafter, all the damage modes spread rapidly, especially the yarn *L* tensile failure, yarn *Z* tensile shear failure and matrix damage, which lead to a sudden drop of the stress-strain curve and the material exhibits brittle fracture characteristics. After  $\bar{\epsilon}_z = 0.60\%$ , due to the failure of yarns, resin matrix bears greater amount of loads. Therefore, the number of damaged elements of matrix cracking ascends faster than other damage modes.

For specimen 2, the main failure modes are yarn *T* compressive shear failure, yarn *Z* tensile shear failure, matrix cracking and interface debonding. At  $\bar{\epsilon}_z = 0.35\%$ , the interface debonding also occurs first in the yarn/yarn contact zones near the top and bottom surfaces

**Table 4** Comparison of predicted results with experiment data

Specimen	Tensile strength (MPa)			Failure strain (%)		
	Prediction <sup>a</sup>	Prediction <sup>b</sup>	experiment data	Prediction <sup>a</sup>	Prediction <sup>b</sup>	experiment data
Specimen 1	459.1	449.0	425	0.60	0.58	0.60
Specimen 2	120.6	121.2	99	0.91	0.89	0.59

<sup>a</sup> indicates with interface

<sup>b</sup> indicates without interface

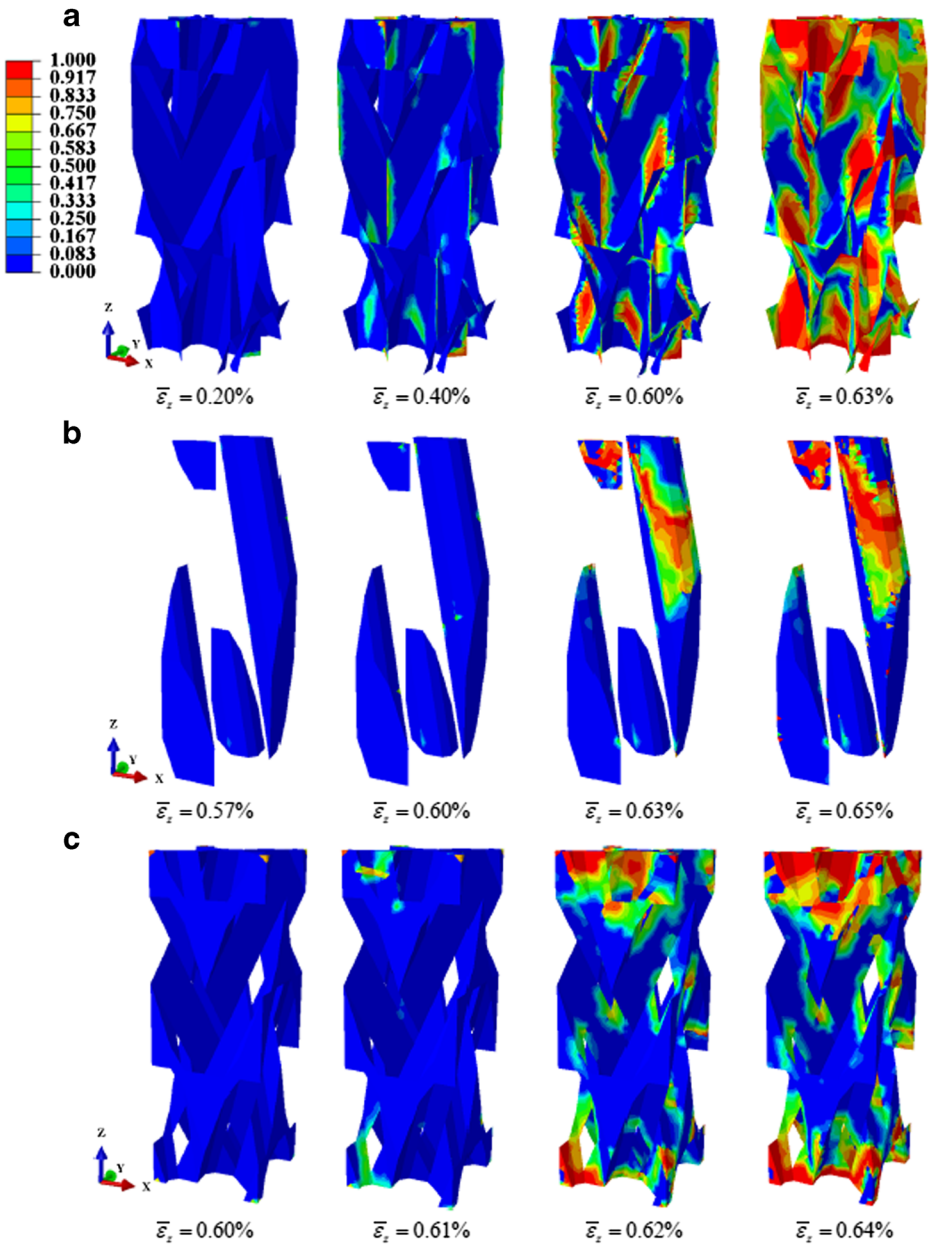


**Fig. 6** Damage evolution process of Specimen 1 under different axial strains **a** Interface debonding **b** Yam *L* tensile failure **c** Matrix cracking

of the unit-cell, as shown in Fig. 7a. Then the interface debonding mainly arises in the yarn/ yarn contact zones inside the unit-cell model, and the interface damage progressively extends along the fiber axial and transverse directions and the extension rate is steady. Damaged elements are less in the yarn/matrix contact zones. Seen from Fig. 7b, the yarn *T* compressive shear failure first initiates in the interlaced regions of braiding yarns and propagates along the



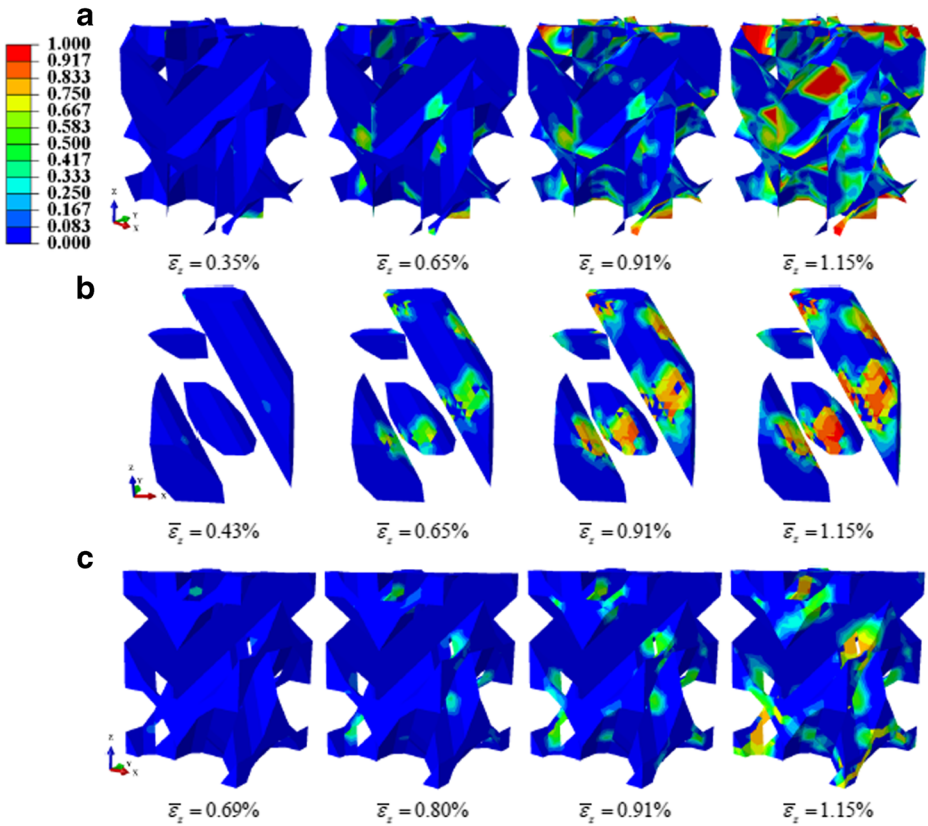


**Fig. 7** Damage evolution process of Specimen 2 under different axial strains **a** Interface debonding **b** Yarn *LT* tensile shear failure **c** Matrix cracking

transverse direction of the braiding yarn, and the propagation speed is fast. The matrix damage first appears in the intersecting edges of the braiding yarn and matrix and expanded gradually in the intersection regions, as shown in Fig. 7c. With the increase of tensile load, various failure modes occur, propagate and couple with each other progressively, which lead to the nonlinear feature of the stress-strain curve. At  $\bar{\varepsilon}_z = 0.91\%$ , the stress-strain curve reaches the maximum value. Compared to specimen 1, the value of uniaxial tensile strength of specimen 2 is relatively small. Under further loading, all kinds of damage modes extend steadily and the stress-strain curve gradually decreases. The material maintains a certain load-bearing capacity and shows certain ductility characteristics.

### 5.3 Parameter Study

Selecting proper material parameters to correctly represent the mechanical response of 3D braided composites is a very difficult task in the finite element modeling. In the above section, the validity of constituents' material parameters in numerical simulation is proved by comparisons with experimental results. In this section, to understand how these key material parameters such as shear failure coefficient, interface strength and fiber volume fraction, contribute to the effective stress-strain curves, a parametric study is conducted. Note that the change of fiber

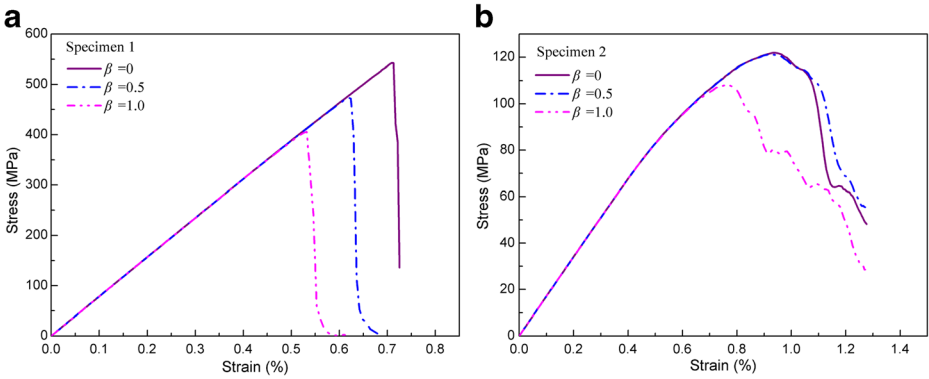


**Fig. 8** Effect of shear failure coefficient on predicted stress-strain curves **a** Specimen 1 **b** Specimen 2

volume fraction in the RUC model is realized by setting different yarn packing factors within a reasonable range.

### 5.3.1 Shear Failure Coefficient

Figure 8 displays the effect of shear failure coefficient on the predicted stress-strain curves. From Fig. 8, it is seen that all the predicted stress-strain curves meet well with each other in modulus but give different strength prediction values. In Fig. 8a, the predicted strength decreases sharply as the shear failure coefficient  $\beta$  increases. In Fig. 8b, the predicted strengths are nearly same when  $\beta = 0$  and  $\beta = 0.5$  but very small when  $\beta = 1.0$ . This is due to the influence of shear stress on the axial breaking of braiding yarns. For 3D braided composites, the braiding yarns are inclined to the  $z$  axis of composites with interior braiding angle. Relatively larger shear stresses are generated in the braiding yarns under axial tension load. With the shear failure coefficient  $\beta$  increases, larger shear stresses will be more likely to cause fiber breakage of braiding yarns. For 3D braided composites with small braiding angle, the tensile strength is controlled by yarn  $L$  tensile failure and thus larger shear failure coefficients will result in lower strength. For 3D braided composites with large braiding angle, when  $\beta = 0$  and  $\beta = 0.5$ , the main failure modes are yarn  $T$  compressive shear and  $Z$  tensile shear failure

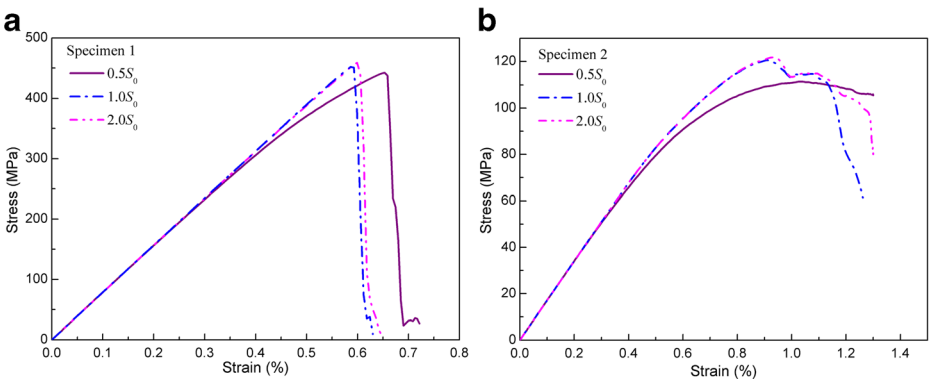


**Fig. 9** Effect of interface strength on predicted stress-strain curves **a** Specimen 1 **b** Specimen 2

without any yarn  $L$  tensile failure. When  $\beta = 1.0$ , yarn  $L$  tensile failure occurs and results in low strength prediction value.

It can be concluded that the shear failure coefficient plays a key role on the stress-strain response prediction of 3D braided composites and different coefficients can be used to calculate the contribution of shear stresses to the axial tensile failure of braiding yarns.

### 5.3.2 Interface Strength

In this section, the strength parameters of interface in Table 3 are termed as base strength  $S_0$ . In order to study the effect of interface strength, three different strengths,  $0.5S_0$ ,  $S_0$  and  $2.0S_0$ , are used. Figure 9 presents the effect of interface strength on the predicted stress-strain curves of 3D braided composites. From Fig. 9, it could be observed that weaker interface strengths lead to lower predicted strengths of the composites and vice versa. Herein, for both specimen 1 and 2, the interface debonding would initiate earlier if the interface strength is weaker and stimulate other types of damage in yarns and matrix. However, since the effective stress-strain behavior of 3D braided composites is mainly determined by the braiding yarns other than the interface, provided the interface strength is not too low, the effect of interface strength on the predicted stress-strain response is not very significant. Due to the different damage mechanisms of braiding yarns under axial tension load, the interface strength effect on specimen 2 with a large braiding angle is more remarkable than that on specimen 1. When the interface strength increases, the damage of interface elements becomes less and even no debonding damage emerges before the fracture of the specimen.

Moreover, it should be pointed out that although the effect of interface strength on the predicted stress-strain response is not evident, it has significant influence on the damage evolution of interface elements and thus it must be considered in the meso-scale finite element modeling.

### 5.3.3 Fiber Volume Fraction

Fiber volume fraction is another important structural parameter which controls the overall mechanical properties of 3D braided composites. Figure 10 illustrates the effect of fiber volume fraction on the predicted stress-strain curves. From Fig. 10a, it is observed that the fiber volume fraction has vital influence on the tensile modulus, strength and failure strain of 3D braided composites with small braiding angle. The tensile modulus and strength increase

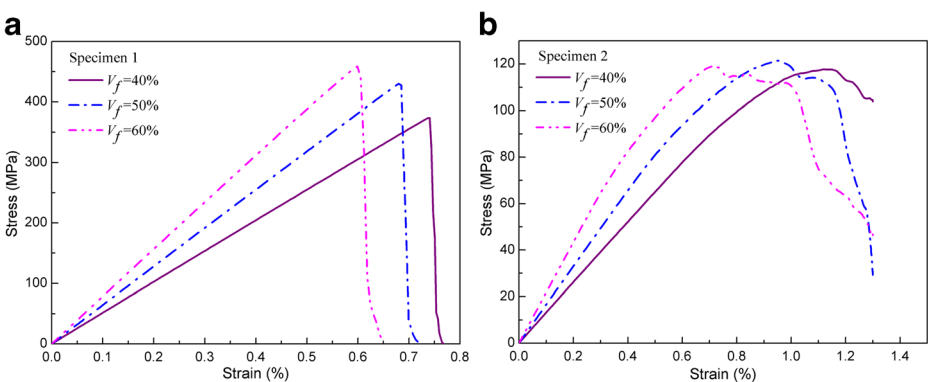


**Fig. 10** Effect of fiber volume fraction on predicted stress-strain curves **a** Specimen 1 **b** Specimen 2

gradually with the increase of fiber volume fraction. In contrast, the failure strain decreases as the fiber volume fraction increases. Similarly, Fig. 10b shows that for 3D braided composites with large braiding angle, the tensile modulus increases while the failure strain decrease as the fiber volume fraction increases. However, the effect of fiber volume fraction on the predicted strength is not very evident. This is because that the strength of 3D braided composites with large braided angle is mainly determined by the transverse strength and shear strength of braiding yarns, which are relatively less influenced by the variation of fiber volume fraction.

In general, the effects of fiber volume fraction on the tensile modulus and failure strain of 3D braided composites are always significant. However, for the effect on the predicted strength, it is obvious when the braiding angle is small and not evident when the braiding angle is large.

## 6 Conclusions

In this paper, a RUC-based finite element model including three phases: braiding yarn, matrix and interface, is established to simulate the damage evolution and predict the tensile properties of 3D braided composites under quasi-static axial tension. 3D Hashin criterion and maximum stress criterion with a gradual degradation scheme are applied to predict the damage evolution of yarns and matrix, while a damage-friction combination interface constitutive model is proposed to capture the interface debonding behavior. A user-material subroutine (VUMAT) involving all the damage models of constituents is coded in the finite element software ABAQUS/Explicit. Two specimens with typical braiding angles are selected to verify the proposed modeling strategy. The whole process of damage evolution of 3D braided composites under quasi-static axial tension is simulated and the damage mechanisms are revealed in the simulation process. According to the simulation results, the main failure modes of 3D braided composites with a small braiding angle are yarn *L* tensile failure, yarn *Z* tensile shear failure, matrix cracking and interface debonding; the main failure modes of the composites with a large braiding angle are yarn *T* compressive shear failure, yarn *Z* tensile shear failure, matrix cracking and interface debonding. By adopting the averaging method, the effective stress-strain curves are predicted, from which the ultimate strength and failure strain are obtained. The numerical results show good agreement with the available experimental results and the effectiveness of the damage simulation model is verified. In addition, the effects of shear failure coefficient, interface strength and fiber volume fraction on the macroscopic stress-strain response of 3D braided composites are discussed in detail. The numerical results may be helpful for understanding the damage mechanisms of 3D braided composites and optimizing the structural design.

**Acknowledgements** This work was supported by the Fundamental Research Funds for the Central Universities (NS2016015).

## References

1. Zeng, T., Wu, L.Z., Guo, L.C.: A finite element model for failure analysis of 3D braided composites. *Mater. Sci. Eng. A.* **366**(1), 144–151 (2004)
2. Dong, J.W., Feng, M.L.: Asymptotic expansion homogenization for simulating progressive damage of 3D braided composites. *Compos. Struct.* **92**(4), 873–882 (2010)

3. Yu, X.G., Cui, J.Z.: The prediction on mechanical properties of 4-step braided composites via two-scale method. *Compos. Sci. Technol.* **67**(3–4), 471–480 (2007)
4. Fang, G.D., Liang, J., Wang, B.L.: Progressive damage and nonlinear analysis of 3D four-directional braided composites under unidirectional tension. *Compos. Struct.* **89**, 126–133 (2009)
5. Lu, Z.X., Xia, B., Yang, Z.Y.: Investigation on the tensile properties of three dimensional full five directional braided composites. *Comput. Mater. Sci.* **77**, 445–455 (2013)
6. Wang, B.L., Fang, G.D., Liang, J., et al.: Failure locus of 3D four-directional braided composites under biaxial loading. *Appl. Compos. Mater.* **19**(3–4), 529–544 (2012)
7. Zhang, D.T., Sun, Y., Wang, X.M., et al.: Meso-scale finite element analyses of three-dimensional five-directional braided composites subjected to uniaxial and biaxial loading. *J. Reinf. Plast. Compos.* **34**(24), 1989–2005 (2015)
8. Miravete, A., Bielsa, J.M., Chiminelli, A., et al.: 3D mesomechanical analysis of three-axial braided composite materials. *Compos. Sci. Technol.* **66**, 2954–2964 (2006)
9. Zhang, C., Li, N., Wang, W.Z., et al.: Progressive damage simulation of triaxially braided composite using a 3D meso-scale finite element model. *Compos. Struct.* **125**, 104–116 (2015)
10. Wan, Y.M., Wang, Y.J., Gu, B.H.: Finite element prediction of the impact compressive properties of three-dimensional braided composites using multi-scale model. *Compos. Struct.* **128**, 381–394 (2015)
11. Wang, C., Zhong, Y.C., Adakalaraj, P.F., et al.: Strength prediction for bi-axial braided composites by a multi-scale modelling approach. *J. Mater. Sci.* **51**, 6002–6018 (2016)
12. Fang, G.D., Liang, J., Lu, Q., et al.: Effect of interface properties on mechanical behavior of 3D four directional braided composites with large braided angle subjected to uniaxial tension. *Appl. Compos. Mater.* **18**(5), 449–465 (2011)
13. Lu, Z.X., Wang, C.Y., Xia, B., et al.: Effect of interfacial properties on the uniaxial tensile behavior of three-dimensional braided composites. *Comput. Mater. Sci.* **79**, 547–557 (2013)
14. Xu, Y.J., You, T., Du, C.L.: An integrated micromechanical model and BP neural network for predicting elastic modulus of 3-D multi-phase and multi-layer composites. *Compos. Struct.* **122**, 308–315 (2015)
15. Sharma, R., Mahajan, P., Mittal, R.K.: Elastic modulus of 3D carbon/carbon composite using image-based finite element simulations and experiments. *Compos. Struct.* **98**, 69–78 (2013)
16. Chen, L., Tao, X.M., Choy, C.L.: On the microstructure of three-dimensional braided preforms. *Compos. Sci. Technol.* **59**(3), 391–404 (1999)
17. Xu, K., Xu, X.W.: On the microstructure model of four-step 3D rectangular braided composites. *Acta. Mater. Compos. Sin.* **23**(5), 154–160 (2006)
18. Hashin, Z.: Failure criteria for unidirectional fiber composite. *J. Appl. Mech.* **47**, 329–334 (1980)
19. Murakami, S.: Mechanical modeling of material damage. *ASME J Appl. Mech.* **55**, 280–286 (1988)
20. Lapczyk, I., Hurtado, J.A.: Progressive damage modeling in fiber reinforced materials. *Compos. Part A.* **38**(11), 2333–2341 (2007)
21. Zako, M., Uetsuji, Y., Kurashiki, T.: Finite element analysis of damaged woven fabric composite materials. *Compos. Sci. Technol.* **63**(3–4), 507–516 (2003)
22. Camanho, P. P., Davila, C. G.: Mixed-mode decohesion finite elements for the simulation of delamination in composite materials. NASA/TM-2002-211737 (2002)
23. Alfano, G., Sacco, E.: Combining interface damage and friction in a cohesive-zone model. *Int. J. Numer. Methods Eng.* **68**, 524–582 (2006)
24. Xia, Z.H., Zhang, Y.F., Ellyin, F.: A unified periodical boundary conditions for representative volume elements of composites and applications. *Int. J. Solids Struct.* **40**(8), 1907–1921 (2003)
25. Chamis, C.C.: Mechanics of composites materials: past, present and future. *J. Compos. Technol. Res.* **11**(1), 3–14 (1989)
26. Xiu, Y.S.: Numerical Analysis of Mechanical Properties of 3D four-Step Braided Composites. Tianjin Polytechnic University; China, Tianjin (2001)